The Astrophysical Journal, 968:54 (9pp), 2024 June 20 https://doi.org/10.3847/1538-4357/ad4606

Hot Gas Outflow Properties of the Starburst Galaxy NGC 4945

Natalia Porraz Barrera[1], Sebastian Lopez[1,2], Laura A. Lopez[1,2], Adi Foord[3], Dustin D. Nguyen[2,4], Todd A. Thompson[1,2], Smita Mathur[1,2], and Alberto D. Bolatto[5,6]
[1] Department of Astronomy, The Ohio State University, 140 W. 18th Ave., Columbus, OH 43210, USA
[2] Center for Cosmology and AstroParticle Physics, The Ohio State University, 191 W. Woodruff Ave., Columbus, OH 43210, USA
[3] Department of Physics, University of Maryland Baltimore County, 1000 Hilltop Circle, Baltimore, MD 21250, USA
[4] Department of Physics, The Ohio State University, 191 W. Woodruff Ave., Columbus, OH 43210, USA
[5] Department of Astronomy, University of Maryland, College Park, MD 20742, USA
[6] Joint Space-Science Institute, University of Maryland, College Park, MD 20742, USA
Received 2023 December 13; revised 2024 March 29; accepted 2024 April 11; published 2024 June 11

Abstract

We analyze 330 ks of Chandra X-ray imaging and spectra of the nearby, edge-on starburst and Seyfert type 2 galaxy NGC 4945 to measure the hot gas properties along the galactic outflows. We extract and model spectra from 15 regions extending from −0.55 to +0.85 kpc above and below the galactic disk to determine the best-fit parameters and metal abundances. We find that the hot gas temperatures and number densities peak in the central regions and decrease along the outflows. These profiles are inconsistent with a spherical, adiabatically expanding wind model, suggesting the need to include mass loading and/or a nonspherical outflow geometry. We estimate the mass outflow rate of the hot wind to be $1.6\,M_{\odot}\,\mathrm{yr}^{-1}$. Emission from charge exchange is detected in the northern outflow, and we estimate it contributes 12% to the emitted, broadband (0.5–7 keV) X-ray flux.

Unified Astronomy Thesaurus concepts: Galactic winds (572); Starburst galaxies (1570)

1. Introduction

The presence of galactic outflows in star-forming galaxies is well established. These star formation feedback-driven outflows have important effects on their host galaxies, such as distributing metals to the circumgalactic and intergalactic medium, quenching star formation, and affecting the metallicity of the galactic disk (Tumlinson et al. 2017; Mathur 2022). These outflows, also known as galactic winds, are multiphase and can be observed in various wavelengths, each with its own set of constraints (Veilleux et al. 2005, 2020).

NGC 4945 is a nearby ($D = 3.72$ Mpc; Tully et al. 2016) edge-on ($i = 78°$; Ott et al. 2001) galaxy that lies in the Centaurus A/M83 group and is known to host a central starburst (Schurch et al. 2002; Emig et al. 2020) as well as a Seyfert type 2 active galactic nucleus (AGN; Iwasawa et al. 1993). The mass of the central black hole is $M_{\mathrm{BH}} = 1.4 \times 10^6\,M_{\odot}$, and the AGN accretes at 10%–30% of the Eddington rate (Puccetti et al. 2014).

Similar to M82 and NGC 253, NGC 4945 is one of the nearest far-IR galaxies (Heckman et al. 1990) producing large-scale outflows along the galaxy's minor axis. The outflow has been observed at millimeter (Bolatto et al. 2021), optical (Venturi et al. 2017; Mingozzi et al. 2019), and X-ray wavelengths (Schurch et al. 2002; Done et al. 2003; Strickland et al. 2004a, 2004b; Marinucci et al. 2012, 2017). In this paper, we focus on Chandra X-ray observations, constraining the temperature and metallicity gradients of the hot gas ($\sim 10^7$ K) in the outflow.

Previous work on the hot phase of NGC 4945's outflows constrained the temperatures as well as the properties of the central AGN (Schurch et al. 2002; Done et al. 2003). Using XMM-Newton and Chandra observations, Schurch et al. (2002) extracted spectra to identify the emission lines of the outflow and nuclear central region. The central region was fitted with a Compton-reflection component, an iron line, and a hot thermal component, while the outflow region was fitted with three thermal components. Done et al. (2003) measured column densities and temperatures in four regions (one from the nuclear source and three along the outflow) by fitting two temperature MEKAL plasma components in the diffuse regions and an iron line and power law in the nuclear region using Chandra and RXTE data. Marinucci et al. (2017) analyzed the circumnuclear environment of the galaxy to understand the central structure of the source using Chandra observations. Spectra were extracted from five circular circumnuclear regions and were fitted with a model that consisted of a reflection continuum and five emission lines to obtain the energy, flux, and equivalent width values for each of the regions.

In this paper, we follow the analysis of Lopez et al. (2020, 2023) to constrain temperature, density, and metal abundances of the outflow in NGC 4945 using 330 ks of archival Chandra data. Previous works have not constrained the metal abundances in the wind nor have they tested the significance and contribution of charge exchange (CX) to the total X-ray emission in NGC 4945. In CX, ions strip electrons from neutral atoms; in galactic winds, CX occurs as the hot phase interacts with the cooler gas. Previous works on other nearby starbursts M82 and NGC 253 have found that CX can contribute significantly to the total broadband (0.5–7 keV) flux, altering the metal abundance estimates substantially if CX is not considered (Zhang et al. 2014; Lopez et al. 2020, 2023).

This paper is structured as follows. In Section 2, we describe the archival Chandra observations and the procedure to create X-ray images and to extract and model spectra. In Section 3, we present temperature, density, and metallicity profiles as well as geometric constraints on the outflows. In Section 4, we compare our results to previous work on NGC 4945 (Section 4.1) and on other nearby galaxies with starburst-driven outflows, M82 and

Table 1
Chandra Observations

ObsID	Exposure[a] (ks)	Start Date
864	49.12	2000-01-27
13791	39.45	2012-01-10
14412	39.14	2012-04-03
14984	128.76	2013-04-25
14985	68.73	2013-04-20
20997	20.71	2018-04-24

Note. These Chandra data sets, obtained by the Chandra X-ray Observatory, are contained in doi:10.25574/cdc.245.
[a] Exposure time on ObsID 864 before 20 ks were removed for background flaring.

NGC 253 (Section 4.2). We also show how the observed temperature and density profiles in NGC 4945 contrast the predictions of a spherically symmetric, adiabatically expanding wind (Section 4.3). We measure the hot gas outflow rates in Section 4.4, and we quantify the contribution of CX emission to the emitted X-ray flux in Section 4.5. In Section 5, we summarize our findings and outline future work.

Throughout the paper, we assume a distance of 3.72 Mpc to NGC 4945 (Tully et al. 2016) and a redshift of $z = 0.001878$ (Allison et al. 2014).

2. Methods

2.1. Observations and Data Reduction

NGC 4945 has been observed six times by Chandra with the Advanced CCD Imaging Spectrometer (ACIS) from 2000 to 2018 (see Table 1). After removing 20 ks of exposure time from the first observation (ObsID 864) due to background flaring (times when the count rate surpassed 10 count s^{-1}), we obtained a total exposure time of ≈330 ks. Our data reduction was performed using version 4.14 of the Chandra Interactive Analysis of Observations, CIAO (Fruscione et al. 2006).

With the CIAO command *merge_obs*, the six observations were merged into a single broadband (0.5–7.0 keV), exposure-corrected X-ray image, and with the *wavdetect* command, point sources were identified. These point sources were then removed with the *dmfilth* command to construct an image of the diffuse gas associated with NGC 4945's hot outflows.

Figure 1 shows a three-color image of the galaxy. The green and red colors are the galactic disk in Hα (Rossa & Dettmar 2003) and the 2.2 μm infrared (Jarrett et al. 2003), respectively, and the blue is the diffuse hot gas in broadband (0.5–7.0 keV) X-rays, which extends ∼0.85 kpc north and ∼0.55 kpc south from the galaxy's disk. In the galaxy-wide image, X-ray point sources are present, while in the zoomed-in X-ray-only image, these point sources were removed to enable mapping of the diffuse outflows. The gap seen in the southern outflow below the starburst ridge may be due to absorption from the disk along the line-of-sight (Ott et al. 2001).

In Figure 2, we show a two-color X-ray image of NGC 4945, with soft (0.5–2.0 keV) X-rays in red and hard (2.0–7.0 keV) X-rays in blue. The hard X-rays peak in the center of the galaxy due to the presence of an AGN and the hot gas produced by the starburst. By comparison, the soft X-rays are more extended and trace the material outflowing from the disk.

2.2. Spectral Analysis

To constrain the properties of the hot gas, we extracted spectra using the CIAO command *specextract* from several regions defined along the minor axis of the outflow. The data were grouped with a minimum of 10 counts per energy bin. There are 15 total regions, as shown in Figure 3: five southern, two central, and eight northern regions, with dimensions $1\farcs0 \times 0\farcs095$ and areas of $343''$. These dimensions were set in order to achieve at least 500 net counts per region, which allowed us to constrain the electron temperature kT and density n_e. After examining the spectra, we opted to combine regions 4 and 5 (called "regions 4 and 5" hereafter) to increase the signal as a "gap" in the X-rays appears there, likely due to absorption from dense gas along the line of sight, consistent with the presence of CO (2-1) emission in that region (the red in the three-color image in Figure 4).

The spectra were modeled with XSPEC Version 12.12 (Arnaud 1996). We adopted solar abundances from Asplund et al. (2009) and photoionization cross sections from Verner et al. (1996). The XSPEC models used to fit the spectral data varied by region, particularly due to the presence of the AGN. A multiplicative factor (CONST) was included in each region to account for changes in flux/emission measure between the observations. Two absorption components (PHABS*PHABS) per region were also included;[7] the first component accounts for the Galactic absorption in the direction of NGC 4945 (frozen to the value of $N_H^{MW} = 1.38 \times 10^{21}$ cm^{-2}; HI4PI Collaboration et al. 2016), and the second absorption component accounts for NGC 4945's intrinsic absorption $N_H^{NGC4945}$ and was allowed to vary. Models from all regions included at least one optically thin, thermal plasma component (APEC) and a power-law component (POWERLAW).

For three southern and eight northern regions (regions 1–3 and regions 8–15), the power law represents the contribution from unresolved point sources (which account for 29% and 33% of the total X-ray flux in the northern and southern outflows, respectively), and in the central regions, it accounts for the AGN contribution. Regions 4 and 5, 8, and 9 require a Gaussian (GAUSS) component with a centroid fixed at 6.4 keV to model the contributions from the AGN's Fe Kα line. Regions 4 and 5, and 6 require an additional blackbody (BBODY) to model the soft excess from the AGN, and region 7 necessitates an additional thermal plasma component to model the hot starburst-produced gas. The models of regions 6 and 7 include a PEXMON component to account for the Compton reflection of the AGN continuum (Nandra et al. 2007) as well as model the Fe Kα line. The two regions, along with region 4 and 5, also include a third PHABS component to account for AGN-related absorption. The final models are listed in Table 2.

To reliably constrain abundances, about 5000 counts are needed. Thus, to get near this threshold, we made two composite regions, one in the northern and one in the southern outflow. The southern composite region has 4000 counts and constrains abundances to a factor of 2; the northern composite region has 11,400 counts and constrains abundances to 50% of the best-fit values. Regions 1–5 are combined into the southern composite region, and the same procedure was done in the north for regions

[7] We note that we also performed spectral fitting using two XSPEC absorption component tbabs for the Milky Way and NGC 4945 column densities assuming Wilms et al. (2000) solar abundances. We found that the spectral results of all regions were statistically consistent within the errors of those reported in Table 4.

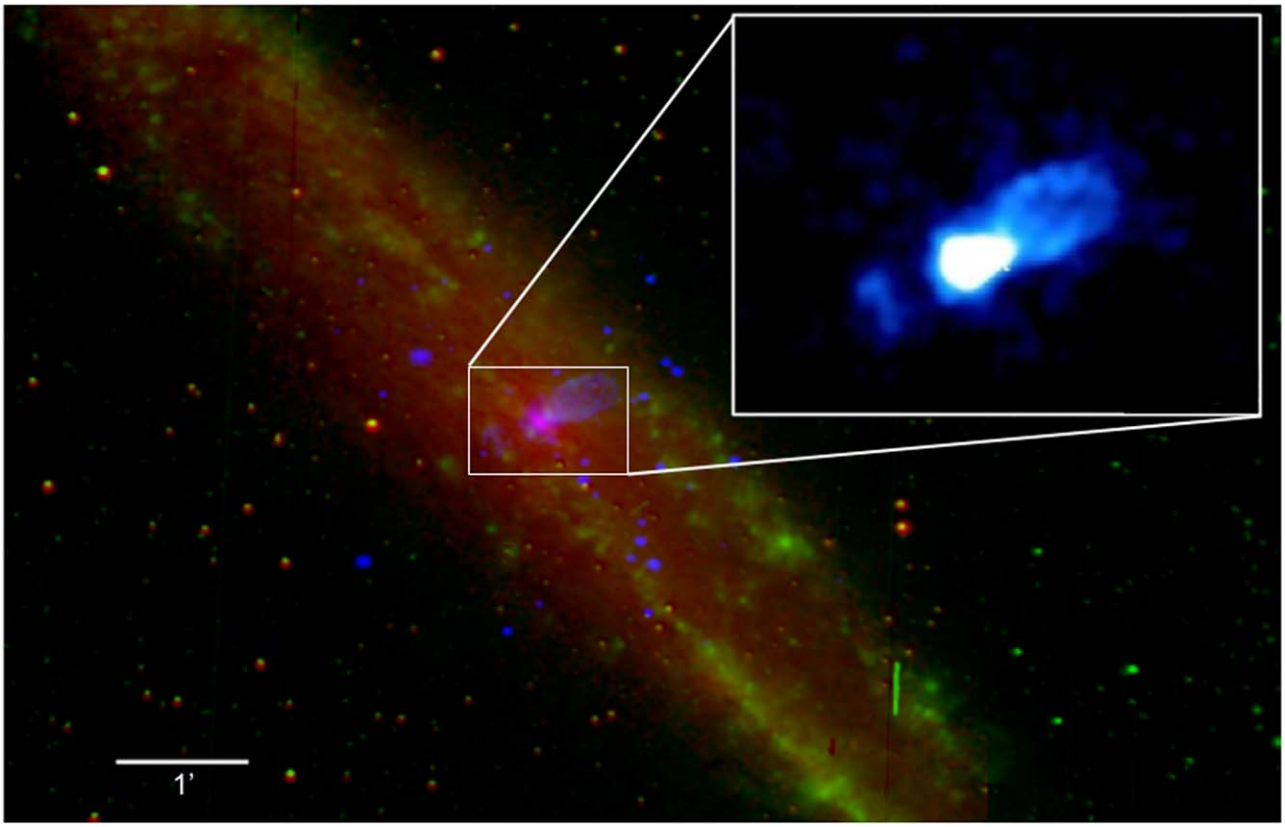

Figure 1. Three-color image of NGC 4945. Blue is the 0.5–7.0 keV Chandra X-rays, green is Hα (Rossa & Dettmar 2003), and red is 2.2 μm infrared (Jarrett et al. 2003) from NASA/IPAC Extragalactic Database (NED; 2019). North is up, and east is left. Zoomed-in picture (top right) shows the diffuse, hot gas of the outflows in X-rays with the point sources removed. At the distance of NGC 4945 1″ is about 1 kpc.

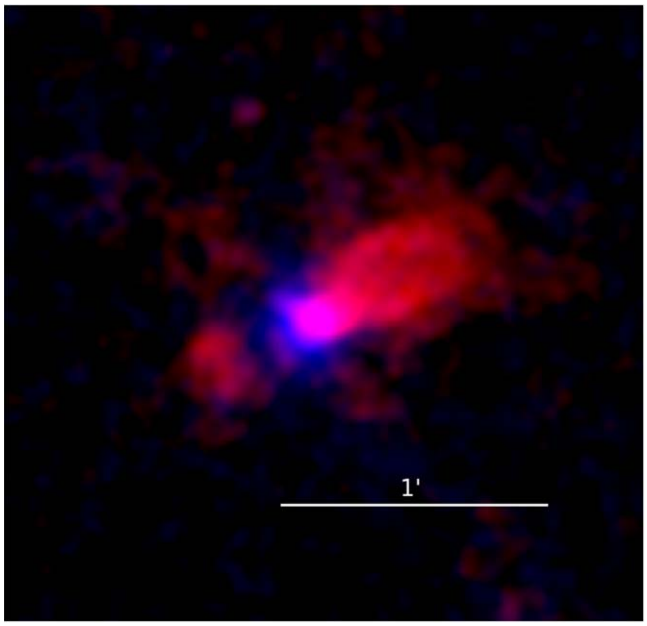

Figure 2. Two-color X-ray image of the soft X-rays (0.5–2.0 keV) in red and the hard X-rays (2.0–7.0 keV) in blue. Hard X-rays are concentrated in the center due to the AGN and starburst activity. The soft X-rays are more extended, trace the outflow, and are absent in the heavily obscured gap region.

8–15. Due to the complex nature of the central regions, we refrain from letting abundances vary there due to a large number of free parameters. We assume the central metallicity is solar based on previous work studying NGC 4945's central super star clusters (SSCs) that power the galactic wind (Emig et al. 2020). The composite southern region has a model of CONST*PHABS*PHABS*(VAPEC+POWERLAW+GAUSS), and the composite northern region has a model of CONST*PHABS*PHABS*(VAPEC+VACX+POWERLAW+GAUSS).

In addition to the components mentioned above, we tested whether the AtomDB CX model component (VACX) is necessary to account for the line emission. CX emission is produced when ions capture electrons from neutral material (Smith et al. 2012), and it has been found to contribute substantially to soft X-rays in starburst-driven outflows (Liu et al. 2011; Lopez et al. 2020, 2023). The inclusion of a CX component statistically improved the spectral fits of the composite northern region. However, the southern region did not need the (VACX) component based on F-tests, likely because of the higher $N_{\rm H}^{\rm NGC4945}$ there. Thus, we did include an ACX component in the northern composite spectrum model but not in the southern model.

3. Results

Figure 3 shows the extracted X-ray spectra from 6 of the 15 regions (two southern, two central, and two northern regions). In region 6 (the southern central region), we detect several emission lines from Mg, Si, S, Ar, Ca, and Fe. Fe Kα is found in four regions (5–8) that are associated with the AGN. Fe XXV (with a centroid energy of ≈6.67 keV) is only apparent in regions 6 and 7 due to the presence of a hotter phase in the starburst there.

Using the models described in Section 2, we fit the spectra and found the best-fit values of the column density $N_{\rm H}^{\rm NGC4945}$,

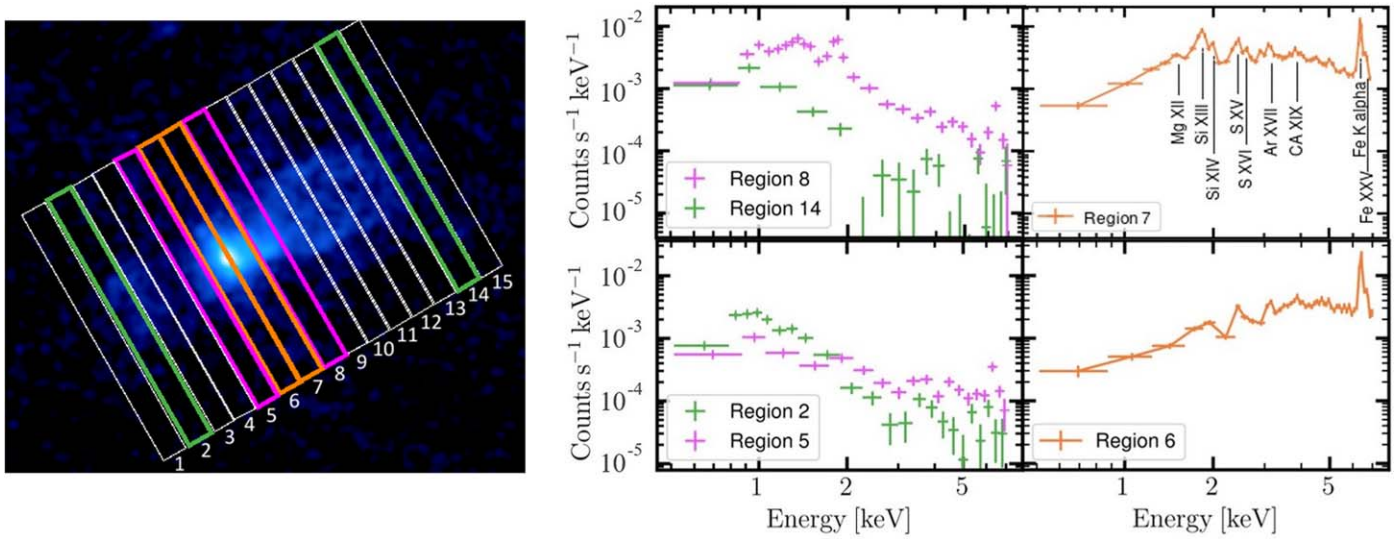

Figure 3. Left: broadband X-ray image of the NGC 4945 outflows with 15 regions overplotted where spectra were extracted. These regions are 1.″0 in height and 0.″095 in width. At the distance of NGC 4945 1′ is about 1 kpc. Right: background-subtracted spectra for 6 of the 15 regions. The top (bottom) row corresponds to the spectra from the northern (southern) regions, 8 and 14 (2 and 5), of the outflow. Emission lines from metals are apparent in the central regions, 6 and 7 (orange), including an Fe Kα line at 6.4 keV and Fe XXV at 6.67 keV. Regions 4 and 5 are located where a "gap" in the southern X-ray outflow is apparent that is coincident with an enhancement in dense gas (see Figure 4) that likely attenuates the X-rays.

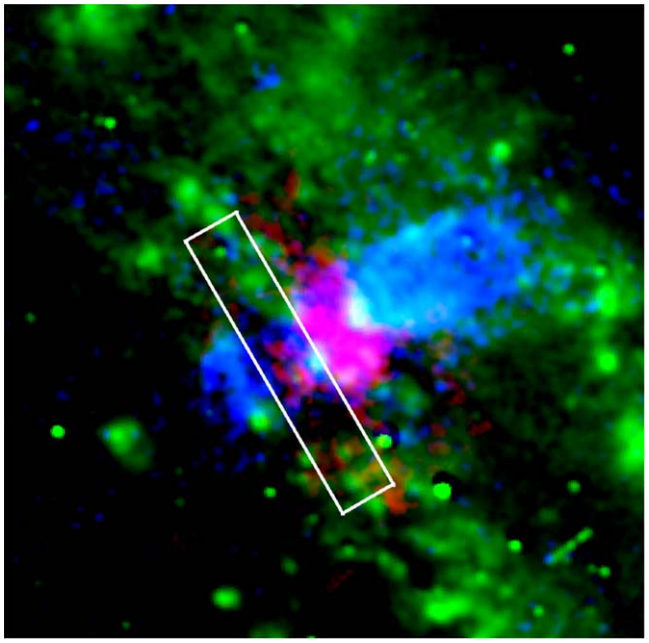

Figure 4. Three-color image of NGC 4945: blue is 0.5–7.0 keV Chandra X-rays, green is Hα (Rossa & Dettmar 2003), and red is CO (2-1) molecular gas (private communication, A. Bolatto). North is up, and east is left. The white box is 1.″0 in height and 0.″19 in width and represents the combined regions 4 and 5 where spectra were extracted (see Figure 3). At the distance of NGC 4945 1″ is about 1 kpc. The gap in X-rays from the southern outflow is coincident with an enhancement of CO (2-1) emission, consistent with the increased column density along the line of sight there.

temperature kT, and metal abundances of the northern (regions 8–15) and southern composite (regions 1–5) regions (see Table 3). The fits yield χ^2/degrees of freedom (dof) of 531/531 for the north and 284/272 for the south. In Table 4 we show the best-fit $N_{\rm H}^{\rm NGC4945}$ and kT for all 15 regions. Both $N_{\rm H}^{\rm NGC4945}$ and kT peak in the center, with $N_{\rm H}^{\rm NGC4945} = (10.1^{+1.99}_{-1.90}) \times 10^{22}$ cm^{-2} and kT=1.04$^{+0.20}_{-0.18}$ keV, and decrease with distance along the outflows in both directions. On average, the southern outflow has higher column densities than the northern outflow due to NGC 4945's disk being along its line of sight, leading to larger uncertainties to the hot gas properties there.

In Table 5 we show the best-fit parameters related to NGC 4945's AGN. These values are the absorbing column $N_{\rm H}^{\rm AGN}$, absorbed power-law slope $\Gamma_{\rm pl}$, and the equivalent widths of the Fe Kα line.

From the best-fit values, we calculate other properties of the outflow for each region, such as the electron number density $n_{\rm e}$, the thermal pressure P/k, and the cooling time $t_{\rm cool}$. The electron number density $n_{\rm e}$ of the thermal plasma is estimated using the best-fit normalizations norm of the APEC components, where norm $= (10^{-14}{\rm EM})/4\pi D^2$ and the emission measure is EM $= \int n_{\rm e} n_{\rm H} dV$. We set $n_{\rm e} = 1.2 n_{\rm H}$, integrate over the volume V, and calculate $n_{\rm e}$ given $n_{\rm e} = (1.5 \times 10^{15} {\rm norm} D^2/fV)^{1/2}$, where f is the filling factor that we assume is $f = 1$.

To compute V for each region, we assume that each region has a cylindrical volume of radius R that is estimated based on the broadband X-ray (0.5–0.7 keV) surface-brightness profiles along the outflows' major axis. R is defined as the scale encompassing 68% of the X-ray surface brightness; this percentile captures most of the observed outflow emission and traces structure well.

The thermal pressure is computed as $P/k = 2 n_{\rm e} T$, and the cooling time is $t_{\rm cool} = 3kT/\Lambda n_{\rm e}$. Λ is the radiative cooling function (in units of erg^{-1} cm^{-3}) calculated using CHIANTI (Dere et al. 1997), assuming a thin, thermal plasma at solar metallicity.

The resulting $n_{\rm e}$, P/k, and $t_{\rm cool}$ for all 15 regions are listed in Table 4. The thermal pressure peaks in the center, specifically in region 7 with value $P/k = 1.9 \times 10^7$ K cm^{-3}, with elevated pressures in regions 6 ($P/k = 2.1 \times 10^7$ K cm^{-3}) and 8 ($P/k = 1.0 \times 10^7$ K cm^{-3}) as well. In the southern regions, the values vary from (1 to 2.6) $\times 10^6$ K cm^{-3}, and in the northern regions they vary from (0.06 to 2.9) $\times 10^6$ K cm^{-3}, decreasing with distance from the starburst disk. The longest

Table 2
Spectral Models

Region	Model
1–3, 10–15	CONST * PHABS * PHABS * (APEC+POWERLAW)
4 and 5	CONST * PHABS * PHABS * (APEC+ BBODY + PHABS * (POWERLAW + GAUSS))
6	CONST * PHABS * PHABS * (APEC+ BBODY + PHABS * POWERLAW + PEXMON)
7	CONST * PHABS * PHABS * (APEC+APEC + PHABS * POWERLAW + PEXMON)
8, 9	CONST * PHABS * PHABS * (APEC+POWERLAW+GAUSS)

Table 3
Spectral Fit Results[a]

Reg.	r (kpc)	$N_{\rm H}^{\rm NGC4945}$ ($\times 10^{22}$ cm^{-2})	kT (keV)	O/O$_\odot$	Ne/Ne$_\odot$	Mg/Mg$_\odot$	Si/Si$_\odot$	S/S$_\odot$	Fe/Fe$_\odot$	χ^2/dof
North	+0.25	$0.16^{+0.09}_{-0.08}$	0.68±0.04	<0.37	$0.81^{+0.71}_{-0.38}$	$0.87^{+0.53}_{-0.30}$	$1.09^{+0.56}_{-0.32}$	$1.41^{+0.97}_{-0.69}$	$0.22^{+0.11}_{-0.06}$	531/531
South	−0.17	$0.64^{+0.11}_{-0.34}$	$0.34^{+0.15}_{-0.06}$	$0.51^{+2.20}_{-0.24}$	$0.28^{+0.41}_{-0.11}$	$0.16^{+0.34}_{-0.14}$	1	1	$0.15^{+0.14}_{-0.05}$	284/272

Note.
[a] Abundances with values of 1 are frozen to solar values in the fits.

Table 4
Physical Parameters of the NGC 4945 Disk Center and Outflow Regions

Reg.	Distance (kpc)	$N_{\rm H}^{\rm NGC4945}$ ($\times 10^{22}$ cm^{-2})	kT (keV)	norm (cm^{-5})	R ($\times 10^{20}$ cm)	V ($\times 10^{62}$ cm^3)	$n_{\rm e}$ (cm^{-3})	P/k ($\times 10^6$ K cm^{-3})	$t_{\rm cool}$ (Myr)	χ^2/d.o.f.
1	−0.55	$1.23^{+0.40}_{-0.43}$	$0.64^{+0.35}_{-0.32}$	5.27×10^{-5}	8.90	6.90	0.12	1.8	25.5	20/21
2	−0.46	$1.29^{+0.35}_{-0.31}$	$0.32^{+0.17}_{-0.10}$	2.90×10^{-4}	7.26	4.59	0.35	2.6	4.19	59/53
3	−0.36	$1.24^{+0.30}_{-0.41}$	$0.32^{+0.35}_{-0.09}$	3.06×10^{-4}	8.08	5.69	0.33	2.4	4.45	76/66
4 and 5[a]	−0.21	$2.56^{+1.01}_{-0.73}$	$0.81^{+0.19}_{-0.14}$	1.29×10^{-4}	7.94	11.3	0.15	1.4	26.1	145/129
6	−0.06	$10.1^{+1.99}_{-1.90}$	$1.04^{+0.20}_{-0.18}$	3.05×10^{-4}	1.51	0.19	1.74	21	3.30	637/468
7[b]	+0.03	$3.78^{+1.08}_{-0.33}$	$0.88^{+0.22}_{-0.12}$	6.14×10^{-5}	1.64	0.24	0.72	7.4	6.15	679/526
8	+0.13	$1.50^{+0.08}_{-0.08}$	$0.67^{+0.07}_{-0.05}$	1.37×10^{-4}	2.74	0.65	0.64	10	4.90	234/201
9	+0.23	$0.77^{+0.10}_{-0.10}$	$0.55^{+0.07}_{-0.09}$	6.05×10^{-5}	5.20	2.36	0.22	2.9	11.8	111/121
10	+0.33	$0.75^{+0.15}_{-0.10}$	$0.49^{+0.08}_{-0.13}$	3.94×10^{-5}	5.75	2.88	0.16	1.9	15.4	128/105
11	+0.42	$1.07^{+0.13}_{-0.19}$	$0.22^{+0.06}_{-0.03}$	1.21×10^{-4}	6.43	3.62	0.26	1.3	2.24	83/89
12	+0.52	$0.96^{+0.15}_{-0.18}$	$0.24^{+0.06}_{-0.04}$	7.29×10^{-5}	6.84	4.09	0.19	1.1	3.93	98/70
13	+0.62	$1.13^{+0.15}_{-0.19}$	$0.22^{+0.07}_{-0.04}$	8.67×10^{-5}	7.26	4.60	0.19	1.0	3.06	69/64
14	+0.72	$0.79^{+0.27}_{-0.27}$	$0.27^{+0.10}_{-0.07}$	2.84×10^{-5}	9.58	8.02	0.08	0.5	12.8	34/44
15	+0.82	$1.26^{+0.37}_{-0.29}$	$0.13^{+0.06}_{-0.03}$	7.03×10^{-6}	10.4	9.45	0.04	0.06	4.72	28/29

Notes.
[a] Due to low signal in regions 4 and 5, the regions were combined to better constrain the outflow properties.
[b] This region required two thermal plasma components so the listed value is a flux-averaged value. The individual values are $kT_1 = 0.85^{+0.11}_{-0.55}$ keV and $kT_2 = 2.53^{+0.85}_{-0.84}$ keV.

cooling time is in region 4 and 5, with $t_{\rm cool} = 26.1$ Myr. Region 11 has the shortest cooling time of $t_{\rm cool} = 2.24$ Myr.

4. Discussion

4.1. Comparison to Previous Work on NGC 4945

Previous X-ray work on both the nucleus and outflows of NGC 4945 has been performed. A very similar analysis was conducted by Schurch et al. (2002) using 24 ks of XMM-Newton and 50 ks of Chandra X-ray observations (6 times shallower than the data analyzed in this work) of NGC 4945 to study the galaxy's nucleus and surroundings within 1 kpc. They extracted a spectrum from a region of radius 3″ centered on the AGN, and it contained ≈750 net counts that were fitted with a Compton-reflection component, an Fe Kα line at 6.4 keV modeled by a Gaussian, and a hot thermal component.

Table 5
AGN Parameters

Parameter	Region 6	Region 7
$N_{\rm H}^{\rm AGN}$ ($\times 10^{22}$ cm^{-2})	383^{+173}_{-109}	448^{+173}_{-110}
Γ_{pl}[a]	1.9	1.9
EW$_{\rm Fe\ K\alpha}$ (keV)	$0.43^{+0.16}_{-0.17}$	$0.88^{+0.20}_{-0.21}$

Note.
[a] Frozen to 1.9 based on the constraints from Puccetti et al. (2014).

Additionally, they extracted a starburst plus outflow spectrum from an elliptical region that excluded the 3″ nucleus region and contained ≈1600 net counts. The spectrum included emission lines from Kα neutral iron at 6.4 keV and helium-like iron at 6.7 keV. They fit the spectra with three thermal-plasma components with temperatures of 0.60 ± 0.03 keV, 0.87 ± 0.08 keV, and $6.0^{+1.1}_{-0.8}$ keV. We do not detect a third temperature component, our hottest component in region 7, $kT_2 = 2.53^{+0.85}_{-0.84}$ keV, is lower than their hottest component even within the uncertainties. Our northern and central region values are statistically consistent with the AGN and starburst spectral results of Schurch et al. (2002).

In Done et al. (2003), an analysis of NGC 4945 was performed using the ≈50 ks of Chandra data as well as simultaneous Rossi X-ray Timing Explorer, RXTE, observations. Separate spectra were extracted from the nucleus and several starburst/superwind regions. The nuclear spectrum was a hard, broadband continuum (which they modeled as a Compton-reflection continuum) and a Fe Kα emission line at 6.4 keV, consistent with our results.

The spectra from the starburst regions had Fe Kα emission that decreased with distance from the nucleus, and they modeled the data using a neutral reflection component as well as a thermal (MEKAL) plasma model. The best fits showed that column density and temperatures decreased going outward from the nucleus, comparable to the values presented in our work.

Marinucci et al. (2017) focused on the nucleus of the galaxy using 420 ks from five Chandra ACIS-S observations, including three observations used in this paper (ObsIDs 864, 14984, and 14985) plus two with the High-Energy Transmission Grating Spectrometer (HETG spectrometer; ObsIDs 4899 and 4900). We did not analyze the HETG observations as the diffracted photons may blend with diffuse emission of the outflows. Marinucci et al. (2017) extracted spectra from five central circular regions, one in the nucleus and four along the circumnuclear region. The analysis focused on data >3 keV separated into three energy bands: 3–6 keV, 6.2–6.5 keV, and 6.6–7.0 keV. The latter two bands were chosen to map the neutral Fe emission and the ionized Fe lines, respectively. The ionized iron was only found near the nucleus, while the neutral iron was present in both the nucleus and outer regions. This is consistent with our results where the Fe XXV line is observed in the central regions 6 and 7 while the Fe Kα line is observed extending up to region 9. The northernmost region of Marinucci et al. (2017) included starburst-associated emission and required a thermal plasma of temperature $2.0^{+1.5}_{-1.0}$ keV, consistent with our analysis and previous results. We also find that the equivalent widths of the Fe Kα line shown in Table 5 are similar to those of Marinucci et al. (2017).

Marinucci et al. (2017) also found a clump of gas with intense Fe XXV emission ≈40 pc from the nucleus. This clump is roughly at the boundary between our regions 6 and 7 and may be one of the contributors to the Fe XXV line we observe in those regions. This finding showed that there is a complex morphology at the center of NGC 4945 and its surroundings. This may be due to the AGN affecting the nearby environment and may be why our spectral models varied substantially by region.

4.2. Comparison to M82 and NGC 253

The analysis in this paper follows that performed in Lopez et al. (2020) of M82 ($D = 3.6$ Mpc) as well as in Lopez et al. (2023) of NGC 253 ($D = 3.5$ Mpc), two other nearby galaxies with starburst-driven outflows. Lopez et al. (2023) showed that the M82 and NGC 253 hot gas outflows contain the same metals, but their distributions differ with distance from the galactic disks, with the former profiles being flat, while the latter are more centrally peaked.

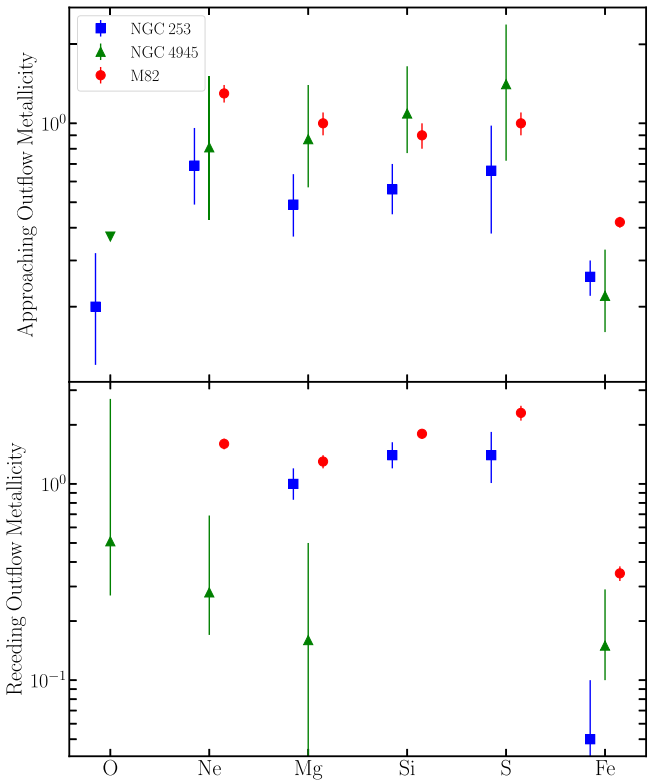

Figure 5. Metal abundances for NGC 4945, NGC 253, and M82 in green triangles, blue squares, and red dots, respectively, at a distance of ∼0.2 kpc from the disk center used for NGC 4945.

NGC 4945 is a third example with starburst-driven galactic outflows. Unlike M82 and NGC 253, NGC 4945 has an AGN, which precludes measurement of metal abundances associated with the central starburst. We did have sufficient signal to measure metal abundances in the composite northern and southern outflow regions (Table 3), but we were not able to produce metal abundance profiles as in M82 and NGC 253.

However, for comparison between these sources, in Figure 5, we plot the metal abundances of these hot gas outflows at the same distance from their galactic disks as measured in NGC 4945. We divide the figure between the approaching outflows (top) and receding outflows (bottom) according to the inclination of these systems. The approaching outflows in M82 and NGC 253 are the southern outflows, while for NGC 4945 it is the northern outflow.

In the approaching outflows, the abundances of NGC 4945, NGC 253, and M82 are statistically consistent with each other where constrained. We find that M82 has higher abundances in the receding outflow for all measured elements (note: oxygen was not constrained in the M82 spectral fits because of the high column density). In the receding outflows, NGC 4945 has the lowest abundances except for Fe; however, the large errors in NGC 4945 (particularly in the receding outflow where the column density is large, attenuating the soft X-ray emission) make comparisons difficult.

The scatter in the receding outflows may be a result of the galactic disk inclination. In all three galaxies, the approaching

outflows have lower column densities compared to the receding ones. This lack of intervening material allows for a higher signal, enabling better constraints on abundances (see Section 2.2). By contrast, the receding outflows have higher column densities, lowering the signal and leading to larger error bars. Consequently, while the receding outflow abundances vary between the galaxies, the large scatter may partly reflect the increased uncertainties in the measurements.

The similarity between the abundances of the galaxies' approaching outflows may be the result of similar outflow driving mechanisms. All three galaxies have star-formation-driven outflows powered by SSCs (Marconi et al. 2000; Melo et al. 2005; Emig et al. 2020; Mills et al. 2021; Levy et al. 2022), and thus their chemical composition reflects the supernova enrichment.

The similar hot gas metallicity profiles of the approaching outflows are noteworthy given the galaxies' different stellar masses. NGC 253 and NGC 4945 have comparable stellar masses of $4.4 \times 10^{10}\,M_{\odot}$ (Bailin et al. 2011) and $3.8 \times 10^{10}\,M_{\odot}$ (Vulic et al. 2018), respectively, while M82 has a stellar mass of $10^{10}\,M_{\odot}$ (Greco et al. 2012). It is observed that lower-mass galaxies have lower metallicity, possibly due to stronger feedback mechanisms ejecting metal-rich gas more efficiently (the stellar-mass–metallicity relation; Tremonti et al. 2004). Chisholm et al. (2018) found that for nearby star-forming galaxies observed in the UV, the metal-loading factor decreases with stellar mass. It is not yet known whether this relationship holds for the hot phase, and it is possible that the lack of variation we find in the approaching outflows between these galaxies is because they do not span a large enough stellar mass range. In the future, X-ray studies of starburst-driven outflows for galaxies that span several dex in stellar mass would be valuable to explore metal loading across gas phases.

4.3. Comparison to Wind Models

The temperature kT and density $n_{\rm e}$ profiles presented in Section 3 can be compared to galactic wind model predictions to constrain outflow properties. The CC85 model presented by Chevalier & Clegg (1985) describes an SN-powered galactic wind that assumes spherical symmetry and adiabatic expansion. This model is useful for comparison to observations because of its simplicity.

In the CC85 model, the starburst radius (R) and the total energy ($\dot{E}_{\rm T}$) and mass-loading ($\dot{M}_{\rm T}$) rates are the only parameters. The energy injection rate into the region defined by R is determined by the equation $\dot{E}_{\rm T} = \alpha \times 3.1 \times 10^{41} \times (\dot{M}_{\rm SFR}/M_{\odot}\ {\rm yr}^{-1})$ [erg s^{-1}], where $\dot{M}_{\rm SFR}$ represents the star formation rate, and α is a dimensionless parameter. The mass-loading rate is given by $\dot{M}_{\rm T} = \beta \times \dot{M}_{\rm SFR}$, where β is another dimensionless parameter. Setting $R = 100$ pc (Marconi et al. 2000) and $\dot{M}_{\rm SFR} = 4.17\,M_{\odot}\ {\rm yr}^{-1}$ (Bendo et al. 2016; adjusted to adopt our assumed distance to NGC 4945), $\alpha \simeq 0.12$ and $\beta \simeq 0.14$.

In Figure 6, we show the measured hot gas temperatures T and electron densities $n_{\rm e}$ (black points) with the CC85 model predictions (red lines) for comparison. Both panels are plotted as a function of distance along the outflow, where $r = 0$ corresponds to the center of the galaxy. When comparing our data with the CC85 model predictions, we find divergence: the measured profiles are broader than those of the models at distances larger than the starburst region of 100 pc.

This discrepancy between the CC85 models and observed hot gas profiles is similar to those found by Lopez et al. (2020) for M82 and by Lopez et al. (2023) for NGC 253. The inclusion of physical processes in the models like mass loading and nonspherical wind geometry is necessary to produce profiles more consistent with observational results (Nguyen & Thompson 2021).

4.4. Mass Outflow Rates

As performed in Lopez et al. (2023), using the estimated electron number density $n_{\rm e}$ and region volume V (listed in Table 4), the mass outflow rates can be calculated. For the southern outflow, we use measurements from regions 1–5, and for the northern outflow, we use measurements from regions 8–15. The mass of the outflows is calculated as $M_{\rm O} = n_e m_{\rm H} V/1.2 f^{1/2}$, where V is the volume of a region and f is the gas filling factor assumed to be 1. The mass outflow rate is then $\dot{M} = M_{\rm O} v/r$, where v is the outflow velocity and r is the vertical distance traveled.

We find a mass of $3.5 \times 10^5\,M_{\odot}$ for the northern outflow and a mass of $4.2 \times 10^5\,M_{\odot}$ for the southern outflow. For the mass outflow rates assuming a hot wind velocity of $v = 10^3$ km s^{-1}, we find a rate of $0.52 v_3\,M_{\odot}\ {\rm yr}^{-1}$ in the northern outflow and $1.1 v_3\,M_{\odot}\ {\rm yr}^{-1}$ in the southern outflow, where v_3 is the outflow velocity in units of 10^3 km s^{-1}. With the assumptions made, the total hot phase outflow mass rate is $1.6\,M_{\odot}\ {\rm yr}^{-1}$, which is less than the cold molecular mass outflow rate of $\sim 20\,M_{\odot}\ {\rm yr}^{-1}$ (Bolatto et al. 2021) and comparable with the ionized phase of $1.6\,M_{\odot}\ {\rm yr}^{-1}$ (Heckman et al. 1990).

4.5. CX Contribution

As described in Section 2, we include a CX component in our spectral fits, and we find it contributes 12% of the total broadband X-ray emission in regions 8–15 of the northern outflow (see Figure 7). CX was not necessary in the spectral models of the southern outflow, likely because of the higher intrinsic column density there obscuring the soft X-rays.

CX, the stripping of an electron from a neutral atom by an ion, contributes significantly to the soft X-ray emission of galactic outflows. Liu et al. (2012) showed that the CX contribution to the Kα triplet of He-like O, Ne, and Mg contributed 90%, 50%, and 30%, respectively, for several nearby starburst galaxies. Across different locations in the M82 outflows, Lopez et al. (2020) found that the CX component contributes up to 25% of the broadband (0.5–7 keV) flux. In the case of NGC 253, up to 42% of the X-ray emission is produced by CX (Lopez et al. 2023).

In our analysis of NGC 4945, we find that the CX component contributes 12% to the broadband flux, which is relatively small compared to the results from M82 and NGC 253. We note that this 12% may be the lower limit on the CX contribution as the high intrinsic column density in NGC 4945 precludes detection of the soft emission where CX is most significant. Recent work by Okon et al. (2023) shows that CX emission in M82 may be concentrated at the interfaces of hot gas with swept-up cool clouds. If the CX arises similarly in the outflows of NGC 4945, then a lower CX flux contribution may suggest lower mass loading and/or smaller cool clouds entrained in the hot superwind.

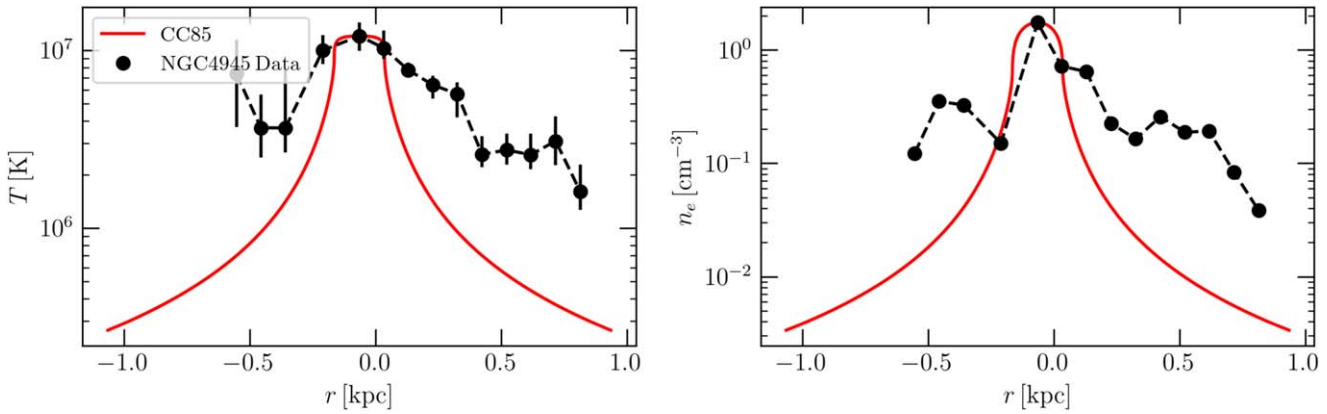

Figure 6. Left: best-fit hot gas temperature T values (black points) as a function of distance along the minor axis from the center of the galaxy (defined as $r = 0$). The red line shows the CC85 adiabatically expanding wind model T prediction. The CC85 parameters used were $R = 100$ pc, $\dot{M}_{\rm SFR} = 4.17\,M_{\odot}\,{\rm yr}^{-1}$, $\alpha \simeq 0.12$, and $\beta \simeq 0.14$. Right: best-fit electron densities $n_{\rm e}$ (black points) compared to CC85 predictions. The measured temperature and density profiles are much broader than predicted, possibly due to mass loading or a nonspherical wind geometry.

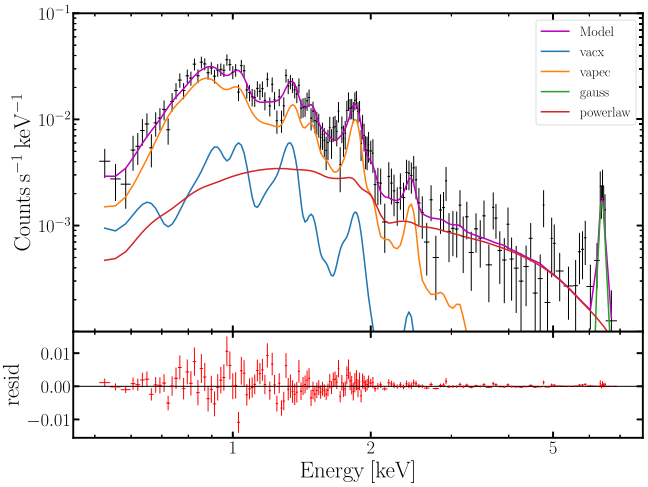

Figure 7. Spectrum from the composite northern region of NGC 4945 (regions 8–15), with the total spectral model, individual model components, and residuals plotted. The VACX component (the blue line) corresponds to the CX emission and contributes 12% to the total 0.5–7 keV emitted flux.

5. Conclusions

We analyze six Chandra observations (totaling 330 ks) of NGC 4945 to obtain images and spectra of the hot galactic outflows extending 0.55 kpc south and 0.85 kpc north from the starburst nucleus where an AGN is present.

We define 15 regions (2 from the galactic disk/starburst and 13 from the outflows; Figure 3) and model their spectra to find the best-fit parameters for the temperatures kT, intrinsic column densities $N_{\rm H}^{\rm NGC4945}$, and electron density $n_{\rm e}$ (Table 4). The temperature and density profiles are broader than predicted from a spherically symmetric, adiabatically expanding wind (Figure 6). These results are consistent with recent work on M82 and NGC 253 and suggest the need to include additional physics in models, such as mass loading and a nonspherical wind geometry.

In addition to this analysis, we also model spectra from composite northern and southern regions of the outflow to derive metal abundances (Table 3). The abundances are greater in the northern outflow than in the southern outflow. The values are consistent with previous work on NGC 253 and M82's outflows (Figure 5). Further X-ray studies are necessary to explore the variation in hot gas metal loading with host galaxy properties.

The northern outflow X-ray spectra require a CX component, which accounts for 12% of the total broadband, emitted X-ray flux (Figure 7). This result adds to a growing body of literature indicating the need to include CX in X-ray spectral models of hot gas in starburst-driven winds.

We also provide an estimate of NGC4945's hot wind mass outflow rate: $1.6\,M_{\odot}\,{\rm yr}^{-1}$ assuming a hot wind velocity of 10^3 km s^{-1}. We do not yet have dynamical information for the hot X-ray gas, but the superb spectral resolution of XRISM (Tashiro et al. 2018) will enable the measurement of hot wind kinematics. Velocity estimates are crucial to obtain better constraints on wind energy and on hot phase mass outflow rates.

Acknowledgments

N.P.B., S.L., and L.A.L. were supported by NASA's Astrophysics Data Analysis Program under grant No. 80NSSC22K0496 and by the Heising-Simons Foundation through grant No. 2022-3533. L.A.L. also acknowledges the support of the Simons Foundation. We thank the OSU Galaxy/ISM Meeting for useful discussions. D.D.N. acknowledges funding from NASA 21-ASTRO21-0174.

Software: XSPEC (Arnaud 1996), CIAO (Fruscione et al. 2006), Astropy (Astropy Collaboration et al. 2013, 2018, 2022).

ORCID iDs

Natalia Porraz Barrera https://orcid.org/0009-0001-0715-7209
Sebastian Lopez https://orcid.org/0000-0002-2644-0077
Laura A. Lopez https://orcid.org/0000-0002-1790-3148
Adi Foord https://orcid.org/0000-0002-1616-1701
Dustin D. Nguyen https://orcid.org/0000-0002-1875-6522
Todd A. Thompson https://orcid.org/0000-0003-2377-9574
Smita Mathur https://orcid.org/0000-0002-4822-3559
Alberto D. Bolatto https://orcid.org/0000-0002-5480-5686

References

Allison, J. R., Sadler, E. M., & Meekin, A. M. 2014, MNRAS, 440, 696
Arnaud, K. A. 1996, in ASP Conf. Ser. 101, Astronomical Data Analysis Software and Systems V, ed. G. H. Jacoby & J. Barnes (San Francisco, CA: ASP), 17

Asplund, M., Grevesse, N., Sauval, A. J., & Scott, P. 2009, ARA&A, 47, 481
Astropy Collaboration, Price-Whelan, A. M., Lim, P. L., et al. 2022, ApJ, 935, 167
Astropy Collaboration, Price-Whelan, A. M., Sipőcz, B. M., et al. 2018, AJ, 156, 123
Astropy Collaboration, Robitaille, T. P., Tollerud, E. J., et al. 2013, A&A, 558, A33
Bailin, J., Bell, E. F., Chappell, S. N., Radburn-Smith, D. J., & de Jong, R. S. 2011, ApJ, 736, 24
Bendo, G. J., Henkel, C., D'Cruze, M. J., et al. 2016, MNRAS, 463, 252
Bolatto, A. D., Leroy, A. K., Levy, R. C., et al. 2021, ApJ, 923, 83
Chevalier, R. A., & Clegg, A. W. 1985, Natur, 317, 44
Chisholm, J., Tremonti, C., & Leitherer, C. 2018, MNRAS, 481, 1690
Dere, K. P., Landi, E., Mason, H. E., Monsignori Fossi, B. C., & Young, P. R. 1997, A&AS, 125, 149
Done, C., Madejski, G. M., Życki, P. T., & Greenhill, L. J. 2003, ApJ, 588, 763
Emig, K. L., Bolatto, A. D., Leroy, A. K., et al. 2020, ApJ, 903, 50
Fruscione, A., McDowell, J. C., Allen, G. E., et al. 2006, Proc. SPIE, 6270, 62701V
Greco, J. P., Martini, P., & Thompson, T. A. 2012, ApJ, 757, 24
Heckman, T. M., Armus, L., & Miley, G. K. 1990, ApJS, 74, 833
HI4PI Collaboration, Ben Bekhti, N., Flöer, L., et al. 2016, A&A, 594, A116
Iwasawa, K., Koyama, K., Awaki, H., et al. 1993, ApJ, 409, 155
Jarrett, T. H., Chester, T., Cutri, R., Schneider, S. E., & Huchra, J. P. 2003, AJ, 125, 525
Levy, R. C., Bolatto, A. D., Leroy, A. K., et al. 2022, ApJ, 935, 19
Liu, J., Mao, S., & Wang, Q. D. 2011, MNRAS: Lett., 415, L64
Liu, J., Wang, Q. D., & Mao, S. 2012, MNRAS, 420, 3389
Lopez, L. A., Mathur, S., Nguyen, D. D., Thompson, T. A., & Olivier, G. M. 2020, ApJ, 904, 152
Lopez, S., Lopez, L. A., Nguyen, D. D., et al. 2023, ApJ, 942, 108
Marconi, A., Oliva, E., van der Werf, P. P., et al. 2000, A&A, 357, 24
Marinucci, A., Bianchi, S., Fabbiano, G., et al. 2017, MNRAS, 470, 4039
Marinucci, A., Risaliti, G., Wang, J., et al. 2012, MNRAS, 423, L6
Mathur, S. 2022, in Handbook of X-ray and Gamma-ray Astrophysics, ed. C. Bambi & A. Santangelo (Berlin: Springer), 59
Melo, V. P., Muñoz-Tuñón, C., Maíz-Apellániz, J., & Tenorio-Tagle, G. 2005, ApJ, 619, 270
Mills, E. A. C., Gorski, M., Emig, K. L., et al. 2021, ApJ, 919, 105
Mingozzi, M., Cresci, G., Venturi, G., et al. 2019, A&A, 622, A146
Nandra, K., O'Neill, P. M., George, I. M., & Reeves, J. N. 2007, MNRAS, 382, 194
NASA/IPAC Extragalactic Database (NED) 2019, NASA/IPAC Extragalactic Database (NED), IPAC, doi:10.26132/NED1
Nguyen, D. D., & Thompson, T. A. 2021, MNRAS, 508, 5310
Okon, H., Smith, R. K., Picquenot, A., & Foster, A. 2023, AAS/HEAD Meeting, 55, 102.32
Ott, M., Whiteoak, J. B., Henkel, C., & Wielebinski, R. 2001, A&A, 372, 463
Puccetti, S., Comastri, A., Fiore, F., et al. 2014, ApJ, 793, 26
Rossa, J., & Dettmar, R. J. 2003, A&A, 406, 505
Schurch, N. J., Roberts, T. P., & Warwick, R. S. 2002, MNRAS, 335, 241
Smith, R. K., Foster, A. R., & Brickhouse, N. S. 2012, AN, 333, 301
Strickland, D. K., Heckman, T. M., Colbert, E. J. M., Hoopes, C. G., & Weaver, K. A. 2004a, ApJS, 151, 193
Strickland, D. K., Heckman, T. M., Colbert, E. J. M., Hoopes, C. G., & Weaver, K. A. 2004b, ApJ, 606, 829
Tashiro, M., Maejima, H., Toda, K., et al. 2018, Proc. SPIE, 10699, 1069922
Tremonti, C. A., Heckman, T. M., Kauffmann, G., et al. 2004, ApJ, 613, 898
Tully, R. B., Courtois, H. M., & Sorce, J. G. 2016, AJ, 152, 50
Tumlinson, J., Peeples, M. S., & Werk, J. K. 2017, ARA&A, 55, 389
Veilleux, S., Cecil, G., & Bland-Hawthorn, J. 2005, ARA&A, 43, 769
Veilleux, S., Maiolino, R., Bolatto, A. D., & Aalto, S. 2020, A&ARv, 28, 2
Venturi, G., Marconi, A., Mingozzi, M., et al. 2017, FrASS, 4, 46
Verner, D. A., Ferland, G. J., Korista, K. T., & Yakovlev, D. G. 1996, ApJ, 465, 487
Vulic, N., Hornschemeier, A. E., Wik, D. R., et al. 2018, ApJ, 864, 150
Wilms, J., Allen, A., & McCray, R. 2000, ApJ, 542, 914
Zhang, S., Wang, Q. D., Ji, L., et al. 2014, ApJ, 794, 61